ISSN 0965-5425, Computational Mathematics and Mathematical Physics, 2006, Vol. 46, No. 5, pp. 848–862. © MAIK "Nauka/Interperiodica" (Russia), 2006.
Original Russian Text © O.N. Koroleva, V.I. Mazhukin, 2006, published in Zhurnal Vychislitel'noi Matematiki i Matematicheskoi Fiziki, 2006, Vol. 46, No. 5, pp. 887–901.

Mathematical Simulation of Laser Induced Melting and Evaporation of Multilayer Materials

O. N. Koroleva[a] and V. I. Mazhukin[b]

[a] *Moscow University of Humanities, Russian Academy of Sciences, pl. Yunosti 5/1, Moscow, 111395 Russia*

[b] *Institute of Mathematical Modeling, Miusskaya pl. 4a, Moscow, 125047 Russia*

e-mail: immras@orc.ru

Received September 9, 2005

Abstract—Using the laser induced remelting of a three-layer target Al + Ni + Cr as an example, the use of the dynamic adaptation for solving the multifront Stefan problem with explicit tracking of the melting and evaporation fronts is considered. The dynamic adaptation is used to construct quasi-uniform grids in regions with moving boundaries. The characteristic size of those regions may vary by several orders of magnitude in the process of computations. The algorithm used to construct the grids takes into account the varying size of the region and the velocity of the boundary motion, which makes it possible to automatically distribute the grid points without using fitting parameters. The mathematical simulation of the doping process using the melt with respect to the thick substrate and thin doping layers showed the importance of the sequencing of coatings. The computations showed that if the upper exposed layer is chromium, then it can completely evaporate or sublimate by the end of the pulse due to its heat-transfer properties. This can be easily changed if the doping layers are arranged according to the scheme Al + Cr + Ni. Then, the upper exposed layer is nickel, which is not so easily evaporated.

DOI: 10.1134/S0965542506050095

Keywords: dynamic adaptation, mathematical simulation, grid generation, difference schemes, phase transitions, laser action, multilayer target, multifront Stefan problem

1. INTRODUCTION

The problem of laser induced remelting of multilayer materials occurs in many technological operations [1]. One of them is connected to laser doping of piston aluminum alloys [2, 3]. This is an important problem because the enhancement of the performance characteristics of pistons is the main way of increasing the lifetime of internal combustion engines. Ever increasing temperatures and dynamic loads lead to the deterioration of the strength properties of the piston in the process of its operation, mainly, due to the deterioration of the grooves under the compression rings. To strengthen those grooves, the aluminum pistons are laser doped with wear-resistant and heat-resistant alloys that improve the microhardness, impact elasticity, wear resistance, and corrosion stability of the metals. The doping is performed with metallic powders based on FeCuB, NiCrMo, or NiCr, which are applied to the piston as coatings and then melted by laser emission (a CO_2 laser with $\lambda = 10.6$ μm) with a relatively small intensity $G \approx 5 \times 10^3$–3×10^4 Wt/cm^2 and the displacement rate $v \approx 0.1$–0.5 m/min. [4, 5]. Then, a groove is made through the remelted region. Studies [6, 7] demonstrated that the powders of Ni and Cr are the most effective dopes. It was established that the quality of the strengthened layer depends not only on the conditions of the laser action but also on the sequence of the doping layers. In particular, it was established that if the upper layer consists of chromium, then the concentration of chromium drops significantly or even completely vanishes after the laser processing.

An adequate solution of this class of problems assumes that such quantities as the surface temperature, the velocity of propagation of the phase front, and the thickness of the melted and evaporated layers are determined. A theoretical investigation of the processes of melting and evaporation under nonstationary conditions can be performed only with the use of mathematical modeling [8].

From the mathematical point of view, the problem under consideration is a nonlinear problem of mathematical physics with strongly varying heat-transfer properties. In the simplest setting, the processes of heating, melting, and evaporation of a multilayer target can be described in the framework of the multifront classical variant of the Stefan problem [8]. From the computational point of view, the main specific features

of this problem are due to the presence of moving interphase boundaries, which must be considered explicitly because of the relevant physical processes.

In this paper, we provide a mathematical model of the laser induced heating, melting, and evaporation of a three-layer metallic target aimed at determining the optimal modes of processing so as to minimize the effect of the evaporation for various sequences of applying the doping layers. The method of dynamic adaptation [8–10] was used to investigate the dynamic behavior of the phase transitions in a multilayer target. An analysis of the modeling results revealed the cause of the absence of the chromium in the remelted samples under certain modes of processing.

2. STATEMENT OF THE PROBLEM

The process called laser doping is based on the phenomenon of the formation of surface layers having a different composition and different properties when the target is coated by an appropriate material, then melted by a laser, and subsequently crystallized. The thickness of the doping depends on the conditions of the laser action; more precisely, it mainly depends on the intensity and duration of the laser pulse. Provided that the duration of the laser pulse is fixed, the intensity is bounded from below by the melting threshold, and it is bounded from above by the appearance of active evaporation.

We use a simplified statement of the problem in which the main role is played by the thermal processes and phase transitions—melting and evaporation—in the three-layer target shown in Fig. 1. The main assumption is that we neglect the hydrodynamic processes due to their great computational complexity. The laser emission is propagating along the axis x from the right to the left (see Fig. 1). When striking the surface of the target, the laser flow is partially absorbed and partially reflected. The absorbed portion of the laser emission depends on the state of the surface; it is characterized by the absorption ability A, which generally depends on the surface temperature.

Depending on the intensity G and on the duration of the action τ_l, the laser emission sequentially causes the heating and then melting or evaporation of all the layers of the target. The first-order phase transitions are characterized by the presence of a sharp interface between the phases. In Fig. 1, the points $x = \Gamma^n_{sl}(t)$ mark the interphase boundaries of the type *solid–liquid*, $x = \Gamma^n_{lv}(t)$ mark the interphase boundaries of the type *condensed medium–vapor*, and $x = \Gamma^{n,n+1}$ mark the contact boundaries between the different media. The superscript n and the subscripts s, l, and v denote, respectively, the nth layer, the solid, liquid, and evaporated material.

For the mathematical description of the processes in multilayer materials exposed to a pulse action, we used the combined variant of the Stefan problem [8] in which the process of melting–solidification is described by the classical Stefan problem, and the evaporation is described in the framework of the single-phase variant. The Stefan problem is solved for a nonlinear heat equation subject to appropriate boundary

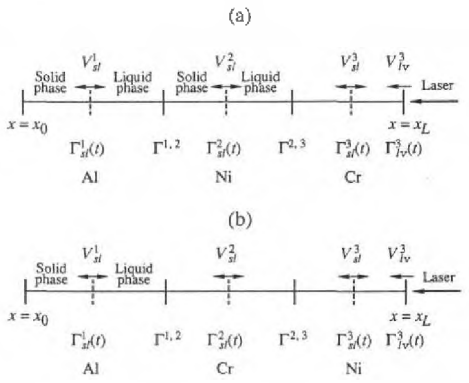

Fig. 1.

conditions:

$$\left[\frac{\partial(\rho H)}{\partial t} = \frac{\partial}{\partial x}\lambda(T)\frac{\partial T}{\partial x}\right]_k^n, \quad H = C_p(T)T, \quad k = s, l, \quad n = 1, 2, 3,$$
$$x_0 < x < \Gamma_{kv}(t), \quad t > 0. \tag{1}$$

Initial and boundary conditions. At the initial instance t_0, the temperature of all the layers is assumed to be equal to a background value T_0:

$$t = t_0 : T(t_0, x) = T_0. \tag{2}$$

The left boundary $x = x_0$ is assumed to be heat-insulated:

$$x = x_0 : \left[-\lambda(T)\frac{\partial T}{\partial x} = 0\right]^1. \tag{3}$$

On the melting–solidification interfaces $x = \Gamma_{sl}^n(t)$, we have two relations, namely, the Stefan condition and the temperature continuity condition:

$$x = \Gamma_{sl}^n(t) : \left[\lambda_s(T)\frac{\partial T_s}{\partial x} - \lambda_l(T)\frac{\partial T_l}{\partial x} = \rho_s L_m v_{sl}\right]^n, \tag{4}$$

$$(T_{sl} = T_s = T_l = T_m)^n, \quad n = 1, 2, 3. \tag{5}$$

On the contact boundaries $x = \Gamma^{n, n+1}$, we have the perfect contact conditions

$$x = \Gamma^{n, n+1} : \left[\lambda(T)\frac{\partial T}{\partial x}\right]^n = \left[\lambda(T)\frac{\partial T}{\partial x}\right]^{n+1}, \quad n = 1, 2, \tag{6}$$

$$T^n = T^{n+1}. \tag{7}$$

On the right exposed boundary $x = \Gamma_{kv}^n(t)$ $(k = s, l)$, the surface evaporation is described using the Knudsen layer [12, 13]:

$$x = \Gamma_{kv}^n(t) : \left[\lambda_k(T)\frac{\partial T_k}{\partial x} - A(T_k)G + \rho_k L_v v_{kv}\right]^n, \tag{8}$$

$$[\rho_k v_{kv} = \rho_v(v_{kv} - u)]^n, \quad [P_k + \rho_k v_{kv}^2 = P_v + \rho_v(v_{kv} - u)^2]^n, \tag{9}$$

$$[T_v = \alpha_T(\mathrm{M})T_k]^n, \tag{10}$$

$$[\rho_v = \alpha_p(\mathrm{M})\rho_H]^n, \tag{11}$$

$$\left[\rho_H = \frac{P_H(T_k)}{RT_k}\right]^n, \quad \left[P_H(T_k) = P_b\exp\left[\left(\frac{1}{T_b} - \frac{1}{T_k}\right)\frac{L_v}{R}\right]\right]^n, \quad n = 1, 2, 3, \quad k = s, l.$$

For M = 1, we have $\alpha_T(\mathrm{M}) = 0.633$ and $\alpha_\rho(\mathrm{M}) = 0.326$; for M = 0, we have $\alpha_T(\mathrm{M}) = \alpha_\rho(\mathrm{M}) = 1$. Here, T_k is the temperature of the condensed medium; $\alpha_T(\mathrm{M})$ and $\alpha_\rho(\mathrm{M})$ are the Crout coefficients; M is the Mach number; R is the gas constant; ρ_H and P_H are the density and the pressure of the saturated vapor; $\lambda(T)$ is the heat conductivity; $C_p(T)$ is the specific heat; H is the enthalpy; L_m and L_v are the transition heats for the melting and evaporation, respectively; v_{sl} and v_{kv} $(k = s, l)$ are the velocities of the melting–solidification and evaporation fronts, respectively; $A(T)$ is the absorption coefficient; $\rho(T)$ is the density; P is the pressure; u is the speed of sound; and T_b and T_m are the boiling and melting temperatures, respectively.

3. THERMOPHYSICAL PROPERTIES AND PARAMETERS

The temperature dependences of the density $\rho(T)$, the specific heat $C_p(T)$, and the heat conductivity $\lambda(T)$ for aluminum, chromium, and nickel were taken from [12–17]; they are represented in Fig. 2. The vertical lines in this figure mark the equilibrium melting and evaporation temperatures for each of the materials.

Note that the thermophysical properties of all the materials have a discontinuity when the equilibrium melting temperature is passed, i.e., when the temperature goes from the values below the equilibrium to higher values or vice versa. In addition, the behavior of the thermophysical properties of the materials considered in this paper is significantly different when the temperature increases.

Chromium and nickel are heavy metals; their density in the solid and the liquid states is 2 to 3 times greater than the density of aluminum: $\rho_{Ni} > \rho_{Cr} \gg \rho_{Al}$ (see Fig. 2a). Accordingly, the propagation velocities of the phase fronts are also very different (they are inversely proportional to the density).

The specific heats of the materials (see Fig. 2b) in the solid state depend on time; in the liquid state, the specific heats are constant. Aluminum has the greatest heat capacity. At room temperature, its specific heat is 2 to 3 times the specific heat of chromium and nickel. With increasing temperature, this difference decreases.

Chromium and nickel don't have very high heat conductivity: it is 2.5–4 times lower than that of aluminum (see Fig. 2c). Pay attention to the maximum jump of the heat conductivity of aluminum (approximately, by a factor of three) when the phase temperature T_m is passed through.

One of the qualitative characteristics of the thermophysical properties of materials is the thermal diffusivity $a = \lambda/C_p\rho$ (see Fig. 3); it describes the depth of the heat influence and the rate of the heat transfer.

In the solid state, the thermal diffusivity of aluminum is greater by a factor of 3–5 than the thermal diffusivity of chromium and nickel. In the liquid state, this factor exceeds 10. Thus, in the process of the laser action, aluminum quickly warms up to a considerable depth, while chromium and nickel warm up to a considerable temperature only near the surface, which manifests itself in the dynamic behavior of the melting–solidification and evaporation processes of the materials in the three-layer target.

The table presents the values of the thermophysical parameters for the materials of interest.

Among these materials, aluminum has the lowest melting temperature $T_m = 933$ K, while chromium has the greatest melting temperature $T_m = 2133$ K. Pay attention to the very low difference between the melting and evaporation temperatures for chromium (less than 40%, $T_b/T_m = 1.38$), while aluminum has $T_b/T_m = 2.99$.

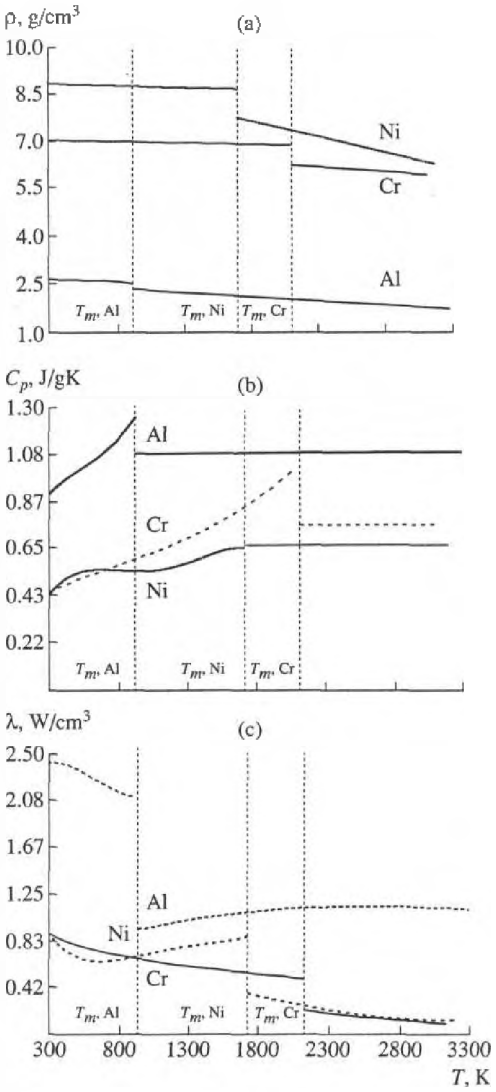

Fig. 2.

4. ALGORITHM OF SOLUTION

To numerically solve problem (1)–(11), we used the dynamic adaptation method [9–11] based on the change to an arbitrary time-dependent system of coordinates with the variables (q, τ) belonging to the computation space $\Omega_{q,\tau}$. When we change to an arbitrary time-dependent system of coordinates, the coordinates of the grid points x_i^j become unknown in addition to the grid functions T_i^j. To determine the new unknowns, we use the inverse transformation equation, which is a partial differential equation. This equation is set up

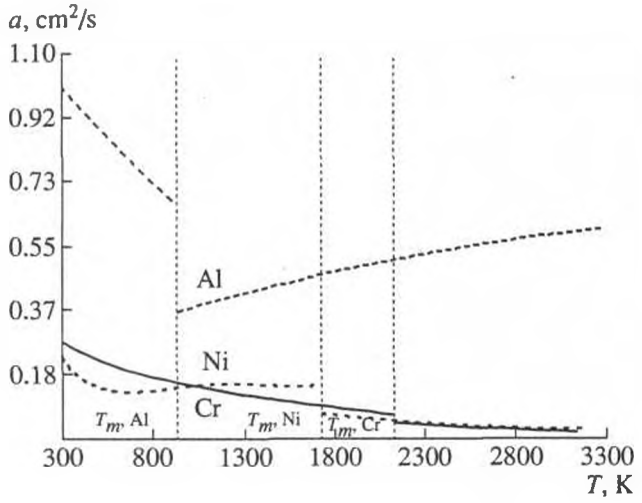

Fig. 3.

in such a way that the velocity of the grid points depends on the dynamic behavior of the equations that describe the physical processes.

4.1. Arbitrary Time-Dependent System of Coordinates

The change from the physical space $\Omega_{x,t}$ to the computation space $\Omega_{q,\tau}$ is performed using the transformation $x = \xi(q, \tau)$, $t = \tau$ that has a nonsingular inverse transformation $q = \varphi(x, t)$, $\tau = t$. The Jacobian of this transformation is $\frac{\psi}{\rho} = \frac{\partial x}{\partial q}$. The partial derivatives of the dependent variables are represented by (see [8–11])

$$\frac{\partial}{\partial t} = \frac{\partial}{\partial \tau} + \frac{Q}{\psi}\frac{\partial}{\partial q}, \quad \frac{\partial}{\partial x} = \frac{\rho}{\psi}\frac{\partial}{\partial q}, \quad \frac{\partial^2}{\partial x^2} = \frac{\rho}{\psi}\frac{\partial}{\partial q}\frac{\rho}{\psi}\frac{\partial}{\partial q},$$

where $\frac{\partial x}{\partial \tau} = -\frac{Q}{\rho}$ is the velocity of the time-dependent system of coordinates and the transformation function Q is unknown in advance and must be determined. In the framework of the problem under consideration, Q is interpreted as the flux of matter: $Q = -\rho v$. In terms of the new variables (q, τ), Eq. (1) is written as

$$\left[\frac{\partial(\psi H)}{\partial \tau} = -\frac{\partial(HQ)}{\partial q} - \frac{\partial W}{\partial q}\right]_k^n, \quad H = C_p T, \quad \left[W = -\frac{\tilde{\lambda}(T)\rho}{\psi}\frac{\partial T}{\partial q}\right]_k^n, \tag{12}$$

$$\left[\frac{\partial \psi}{\partial \tau} = -\frac{\partial Q}{\partial q}\right]_k^n, \quad \left[\frac{\partial x}{\partial q} = \frac{\psi}{\rho}\right]_k^n, \tag{13}$$

where $q_0 < q < \Gamma_{kv}$, $\tau \geq 0$, $n = 1, 2, 3$, and $k = s, l$.

Table

Element	A, g/mol	T_m, K	T_b, K	T_b/T_m	Transition heat	
					melting L_m, J/g	boiling L_b, J/g
Al	26.98	933	2793	2.99	400.3	10860
Cr	52	2133	2953	1.38	313.5	6500
Ni	58.71	1728	3188	1.85	299.8	6302

After changing the coordinates, input equation (1) is transformed into Eq. (12) and is complemented by the inverse transformation equation (13). Upon determining the concrete form of the function Q, Eq. (13) is used to construct the adapting grid. The difference analog of this equation describes the dynamics of the grid points, and Q controls the motion of the grid points, which is consistent with the dynamic behavior of the unknown solution. The consistency can be achieved due to the fact that Q depends on the unknown solution, i.e., on the functions $T(t, x)$, $v_{sl}^n(t)$, and $v_{kv}^n(t)$. A proper choice of Q that ensures the consistency between the solution and the motion of the grid points is the crucial point in the dynamic adaptation method.

Usually, to compensate for the incomplete consistency between the unknown solution and the mechanism of the grid reconstruction, the transformation function is supplied with fitting coefficients, which can be used to reduce the degree of inconsistency. On the other hand, the use of the fitting coefficients indicates that the adaptation method is imperfect.

Initial and boundary conditions. As a result of the change to an arbitrary time-dependent system of coordinates, the coordinates of the grid points x_i^j become new unknowns, in addition to the unknown grid functions T_i^j. To find the new unknowns, the extended mathematical model (12), (13) includes the inverse transformation equation (13), which is a partial differential equation.

The transformation of the input equation (1) into the extended differential system (12), (13) requires additional initial and boundary conditions.

We assume that the change to the computation space is not accompanied by the deformation of the initial domain and, at the initial moment in time, the following conditions are fulfilled:

$$\tau = \tau_0 : T(\tau_0, q) = T_0, \quad \psi = (\tau_0, q) = 1. \tag{14}$$

The left boundary $q = q_0$ is assumed to be heat-insulated and fixed:

$$q = q_0 : -\lambda(T)\frac{\rho}{\psi}\frac{\partial T}{\partial q} = 0, \quad Q(\tau, q_0) = 0. \tag{15}$$

On the melting–solidification interfaces $q = \Gamma_{sl}^n$, we have two relations for the temperature T_{sl}^n and for the flux of matter Q_{sl}^n:

$$q = \Gamma_{sl}^n : (T_{sl} = T_s = T_l = T_m)^n, \tag{16}$$

$$Q_{sl}^n = -\rho_s^n v_{sl}^n = \left\{\left(\lambda(T)\frac{\rho}{\psi}\frac{\partial T}{\partial q}\right)_l^n - \left(\lambda(T)\frac{\rho}{\psi}\frac{\partial T}{\partial q}\right)_s^n\right\}(L_m^n)^{-1}. \tag{17}$$

On the contact boundaries $x = \Gamma^{n, n+1}$, the perfect contact conditions (6) are complemented by the conditions that the boundary is fixed:

$$q = \Gamma^{n, n+1} : \left[\lambda(T)\frac{\rho}{\psi}\frac{\partial T}{\partial q}\right]^n = \left[\lambda(T)\frac{\rho}{\psi}\frac{\partial T}{\partial q}\right]^{n+1}, \quad T^n = T^{n+1}, \tag{18}$$
$$Q^{n, n+1}(\tau, \Gamma^{n, n+1}) = 0.$$

On the right-hand evaporation boundary $q = \Gamma_{kv}^n$ $(k = s, l)$, we used three conservation laws and three additional conditions on the external boundary of the Knudsen layer:

$$q = \Gamma_{kv}^n : \left[\lambda_k(T)\frac{\rho}{\psi}\frac{\partial T_k}{\partial q} = A(T_k)G - L_v Q_{kv}\right]^n, \tag{19}$$

$$\left[Q_{kv} = \rho_v\left(\frac{Q_{kv}}{\rho_k} - u\right)\right]^n, \tag{20}$$

$$\left[P_k + \frac{Q_{kv}^2}{\rho_k} = P_v + \rho_v\left(-\frac{Q_{kv}}{\rho_k} - u\right)^2\right]^n, \tag{21}$$

$$n = 1, 2, 3, \quad k = s, l, \quad T_v = \alpha_T(\mathrm{M})T_k, \quad \rho_v = \alpha_\rho(\mathrm{M})\rho_H,$$

$$\rho_H = \frac{P_H(T_k)}{RT_k}, \quad P_H(T_k) = P_b \exp\left[\left(\frac{1}{T_b} - \frac{1}{T_k}\right)\frac{L_v}{R}\right],$$

$$\begin{aligned} &\text{for M} = 1 \text{ we have } \alpha_T(\text{M}) = 0.633, \quad \alpha_p(\text{M}) = 0.326, \\ &\text{for M} = 0 \text{ we have } \alpha_T(\text{M}) = \alpha_p(\text{M}) = 1. \end{aligned} \tag{22}$$

Here, Q_{sl}, Q_{kv} $(k = s, l)$ is the flux of the matter through the melting–solidification and evaporation boundaries.

4.2. The Transformation Function Q

The inclusion of the temperature dependence $T(t, x)$ in the transformation function makes it possible to have more grid points in the regions where the solution has a large gradient. Based on the belief that a large heat conductivity of metals is not favorable for the formation of temperature regions with large gradients, we may assume that the main specific feature of the Stefan problem is the presence of moving phase fronts. In this case, we can eliminate the dependence of Q on $T(t, x)$. In this case, we can take into account only the propagation velocity of the phase fronts $v_{sl}^n(t)$ and $v_{kv}^n(t)$, and construct the computation grids with a uniform (more precisely, quasi-uniform) distribution of the grid points at every time in the regions with moving boundaries.

In the dynamic adaptation method, the quasi-uniform distribution of the grid points is achieved using a quasi-uniform distribution of the function ψ over the space. At every instant of time, such a distribution can be achieved if the inverse transformation equation is a diffusion-type equation. For this purpose, it is sufficient to represent Q in the form (see [8–11])

$$Q = -D\frac{\partial \psi}{\partial q}, \tag{23}$$

where D is a free parameter interpreted as the diffusion coefficient.

With regard for (23), the inverse transformation equation (13) takes the form

$$\frac{\partial \psi}{\partial \tau} = -\frac{\partial Q}{\partial q} = \frac{\partial}{\partial q} D\frac{\partial \psi}{\partial q}. \tag{24}$$

For sufficiently large values of D, any perturbation of ψ on one of the boundaries or inside the domain will distribute uniformly along the space variable q; upon a difference approximation of the differential model, this ensures a quasi-uniform distribution of the grid points in the physical space $\Omega_{x,t}$ at every moment in time.

Taking into account that the sizes of the domains in the problem under consideration are very different, the method used to determine D is of crucial importance for the construction of the adapting grids.

4.3. Selection of the Coefficient D

Consider the inverse transformation equation (24) in the region bounded by $q_0 = \Gamma_0$ and $q_r = \Gamma_r$. In the physical space, the associated boundaries are the moving boundaries $x_0 = \Gamma_0(t)$ and $x_r = \Gamma_r(t)$, which travel with the speeds v_0 and v_r, respectively. In the case $D = \text{const}$, Eq. (24) is the linear parabolic equation

$$\frac{\partial \psi}{\partial \tau} = -\frac{\partial Q}{\partial q} = D\frac{\partial^2 \psi}{\partial q^2} \tag{25}$$

with the boundary conditions

$$\tau = 0 : \psi(q, 0) = \text{const}, \tag{26}$$

$$\begin{aligned} q_0 = \Gamma_0 &: Q(q, \tau) = v_0, \\ q_r = \Gamma_r &: Q(q, \tau) = v_r. \end{aligned} \tag{27}$$

The solution perturbation $\delta\psi$ can appear on one or both boundaries if v_0 and v_r are distinct from zero. If D is sufficiently large, the solution of problem (25)–(27) is a function that is independent of the space

variable q at every time τ; i.e.,

$$\psi(q, \tau) = \text{const}(\tau). \tag{28}$$

The independence of ψ of the space variable allows us to construct a uniform (more precisely, a quasi-uniform) grid in the physical space. To this end, D must be chosen such that a perturbation appearing on one of the boundaries could reach the opposite boundary in the time Δt; i.e., it must have enough time to travel the distance

$$\Delta x_T = \Gamma_r(t) - \Gamma_0(t) = L(t).$$

The difficulty in the problem is that the size of the region $L(t)$ can vary by several orders of magnitude in the course of time. For example, the newly appearing phase in the melting process has a size of about several Angström units ($L_0 \sim 10^{-8}$ cm), while this size is $L(t_{\text{end}}) \sim (10^0$–$10^1)$ cm at the end of the process. Respectively, the function ψ, which describes the dynamic behavior of the region, varies within the range from $\psi_0 = 1$ at $t = 0$ to $\psi_{\text{end}} = 10^8 - 10^9$ at $t = t_{\text{end}}$.

To find D, we use the linear estimate for parabolic equation (25), which describes the length of the perturbation propagation from one of the boundaries (see [18]):

$$\Delta x_T(t) = (D\Delta t)^{1/2}. \tag{29}$$

Hence, we obtain

$$D = \frac{(\Delta x_T)^2}{\Delta t} = \frac{L^2(t)}{\Delta t}. \tag{30}$$

On the other hand, the expansion of the region due to the motion of the boundaries during the time Δt is

$$\Delta x(t) = (|v_r - v_0|)\Delta t = \Delta L(t),$$

whence we have

$$\Delta t = \frac{\Delta L(t)}{|v_r - v_0|}. \tag{31}$$

Using (31), we can eliminate Δt in (30):

$$D = \frac{L^2(t)}{\Delta L(t)}(|v_r - v_0|). \tag{32}$$

If only one of the boundaries is moving, we have, respectively,

$$D = \frac{L^2(t)|v_0|}{\Delta L(t)} \text{ or } D = \frac{L^2(t)|v_r|}{\Delta L(t)}.$$

In the expressions for D, the size $L(t)$ of the region, which changes in time, can be written as

$$L(t) = \psi(t)L_0,$$

where L_0 is the size of the region at the initial time $t = 0$. Note that, for $\psi(q, 0) = 1$, the size of the domain in the computation and in the physical spaces is the same; i.e., $L_0 = x_r(0) - x_0(0) = q_r - q_0$.

The dynamic increase of the size of the region $\Delta x(t) = \Delta L(t)$ can be represented in terms of the approximate representation of the Jacobian of the transformation

$$\frac{\Delta x}{\Delta q} \equiv \frac{\psi}{\rho}, \quad \Delta x(t) = \Delta L(t) = \frac{\psi}{\rho}\Delta q.$$

Substitute the relations for $L(t)$ and $\Delta L(t)$ into (32) to obtain the final formula for D in terms of the parameters of the input problem—the geometric size of the region $L(t)$ and the speeds of the boundaries v_0 and v_r:

$$D = \frac{L^2(t)}{\Delta L(t)}(|v_r - v_0|) = \frac{\psi L_0^2}{\Delta q \rho}(|v_r - v_0|). \tag{33}$$

Thus, the elimination of the fitting coefficient D enables us to make the construction of the quasi-uniform grids fully automatic independently of the linear size of the domain and the speed of the boundaries.

4.4. Difference Approximation of the Differential Model in the Computation Space

In the computation space $\overline{\Omega}_{q,\tau}$, the grid with the set of points $(\omega_q^\tau)_k^n$ is defined. The set of grid points is indexed using integer indexes i and half-integer indexes $i + 1/2$. The grid has the constant size h with respect to the space variable q and the variable size $\Delta\tau^j$ with respect to τ:

$$\{\omega_q^\tau = [(q_i, \tau^j), (q_{i+1/2}, \tau^j), q_{i+1} = q_i + h, q_{i+1/2} = q_i + 0.5h, i = 0, 1, \ldots, N-1,$$
$$\tau^{j+1} = \tau^j + \Delta\tau, j = 0, 1, \ldots]\}_k^n.$$

In the physical space $\overline{\Omega}_{x,t}$, in accordance with the grid $(\omega_q^\tau)_k^n$, we define the grid $(\omega_x^t)_k^n$ with the set of points indexed by the integers (x, t^j) and half-integers $(x_{i+1/2}, t^j)$ with the constant size h_x with respect to the space variable x and the variable size Δt^j with respect to t:

$$\{\omega_x^t = [(x_i, t^j), (x_{i+1/2}, t^j), x_{i+1} = x_i + h_x, x_{i+1/2} = x_i + 0.5h, i = 0, 1, \ldots, N-1,$$
$$t^j = t^j + \Delta t^j, j = 0, 1, \ldots]\}_k^n.$$

In the computation space, the integer grid points (q_i, τ^j) are associated with the flux quantities W_i^j, Q_i^j and the variable x_i^j. The half-integer grid points $(q_{i+1/2}, \tau^j)$ are associated with the grid functions $T_{i+1/2}^j$, $\rho_{i+1/2}^j$, and $\psi_{i+1/2}^j$.

The system of differential equations (12), (13) is approximated by the system of conservative difference schemes (see [19])

$$\left[\frac{(\psi H)_{i+1/2}^{j+1} - (\psi H)_{i+1/2}^j}{\Delta\tau^{j+1}} = -\frac{(QH)_{i+1}^{j+1} - (QH)_i^j}{h_i} - \frac{W_{i+1}^{j+1} - W_i^j}{h_i}\right]_k^n,$$

$$\left[\frac{\psi_{i+1/2}^{j+1} - \psi_{i+1/2}^j}{\Delta\tau^{j+1}} = -\frac{Q_{i+1}^{j+1} - Q_i^{j+1}}{h_1}\right]_k^n,$$

$$\left[\frac{x_{i+1}^{j+1} - x_i^{j+1}}{h_1} = \frac{\psi_{i+1/2}^{j+1}}{\rho_{i+1/2}^{j+1}}\right]_k^n, \quad \left[Q_i^j = -D_i^j \frac{\psi_{i+1/2}^j - \psi_{i+1/2}^j}{0.5(h_i + h_{i-1})}\right]_k^n, \tag{34}$$

$$\left[W_i^j = -\frac{\lambda_i^j \rho_i^j}{\psi_i^j} \frac{T_{i+1/2}^j - T_{i-1/2}^j}{0.5(h_i + h_{i-1})}\right]_k^n, \quad i = 1, 2, \ldots, N-1.$$

Boundary conditions (14)–(22) are approximated by the following finite difference relations:

$$q = q_0 : W_0^j = 0, \quad Q_0^j = 0,$$

$$q = \Gamma_{sl} : (T_s^j = T_s^j = T_l^j = T_m)^n, \quad \left(Q_{sl}^j = -\rho_s^j v_{sl}^j = \frac{W_l^j - W_s^j}{L_m}\right)^n,$$

$$q = \Gamma^{n,n+1} : (W^j)^n = (W^j)^{n+1}, \quad (T^j)^n = (T^j)^{n+1}, \quad (Q^j)^{n+1} = 0, \tag{35}$$

$$q = \Gamma_{kv}^n : \left[\lambda_i^j \frac{\rho_i^j}{\psi_i^j} \frac{T_{i+1/2}^j - T_{i-1/2}^j}{0.5(h_i + h_{i-1})} = A_k^j G^j - L_v Q_{kv}^j\right]^n,$$

$$[Q_{kv}^j = \rho_v((\rho_k^j)^{-1} Q_{kv}^j - u^j)]^n, \quad [P_k^j + (\rho_k^j)^{-1}(Q_{kv}^j)^2 = P_v^j + \rho_v^j((-\rho_k^j)^{-1} Q_{kv}^j - u^j)^2]^n$$
$$[T_v^j = \alpha_T(\mathrm{M}) T_k^j]^n, \quad [\rho_v^j = \alpha_\rho(\mathrm{M}) \rho_H^j]^n,$$

$$\left(\rho_H^j = \frac{P_H^j}{RT_k^j}\right)^n, \quad \left[P_H^j = P_b \exp\left[\left(\frac{1}{T_b} - \frac{1}{T_k^j}\right)\frac{L_v}{R}\right]\right]^n. \tag{36}$$

System of difference equations (14), (35) is linearized and then solved by the separate sweep method with iterations [20].

5. SIMULATION RESULTS

We focused on the investigation of the dynamics of heating and phase transitions in the three-layer target consisting of a thick aluminum substrate (l_{Al} = 0.5–1 cm) and two thin coatings of nickel and chromium ($l_{Ni} = l_{Cr}$ = 10–50 μm heated by a long laser pulse (τ_l = 1–5 s) with a rectangular time profile and relatively small intensity ($G = (3 \times 10^5)$–(3×10^4) W/cm^2). The choice of the exposure conditions and the geometric and thermophysical parameters of the materials was correlated with the data of the technological experiments [6, 7]. According to the experimental studies [4–7], such exposure regimes correspond to deep melting of all the layers of the target in the absence of the intensive surface evaporation.

Consider the typical example of laser treatment of the three-layer target with the layers of thickness l_{Al} = 0.5 cm and $l_{Ni} = l_{Cr}$ = 25 μm. The duration and intensity of the laser pulse were τ_l = 4 s and G = 10^4 Wt/cm^2. Two configurations of the three-layer target were investigated for melting and evaporation. In the first configuration (see Fig. 1a), the upper doping layer was chromium, and in the second one, it was nickel (Fig. 1b).

In both cases illustrated in Fig. 1, the laser emission strikes the surface of the upper coating and is partially reflected. The absorption capacity of the metallic surface was assumed to be independent of the temperature and equal to A = 0.1, which corresponds to the absorption of the laser emission with the wavelength $\lambda_l \approx$ 10.6 μm. The absorbed portion of the laser pulse is completely released in the upper layer and quickly heats it. The second layer and the aluminum substrate are heated due to heat conduction. The aluminum substrate is the first to melt because it has the lowest melting temperature T_m (see Fig. 4a). Then, nickel is melted. Chromium, which has the highest melting temperature T_m, is the last to melt (see Fig. 4a). Since aluminum has the largest jump of the heat conductivity on the interphase boundary Γ_{sl} and the lowest density, it has the highest melting rate $v_{sl,\max} \approx$ 0.58 cm/s. At such a rate, the substrate completely melts in the time $\Delta t \approx$ 1.2 s, which is much shorter than is required for nickel and chromium to begin melting.

In the scheme depicted in Fig. 1a, where the exposed layer consists of chromium, even before the chromium begins to melt (more precisely, start-

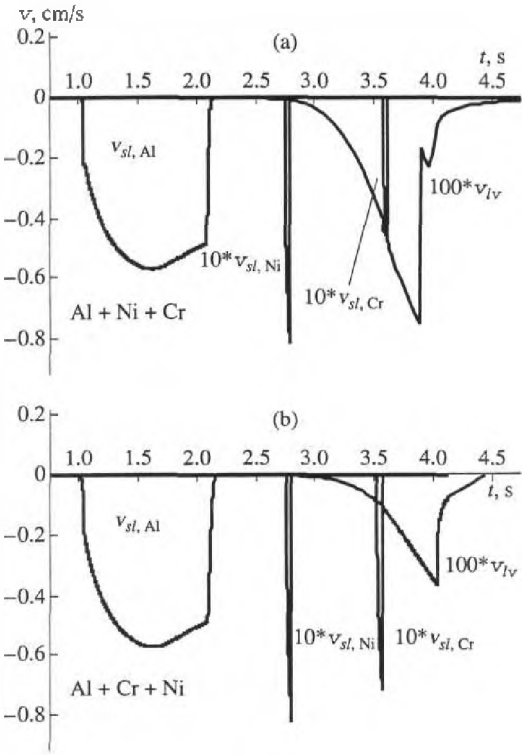

Fig. 4.

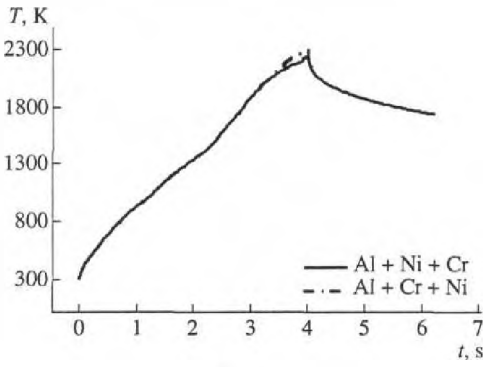

Fig. 5.

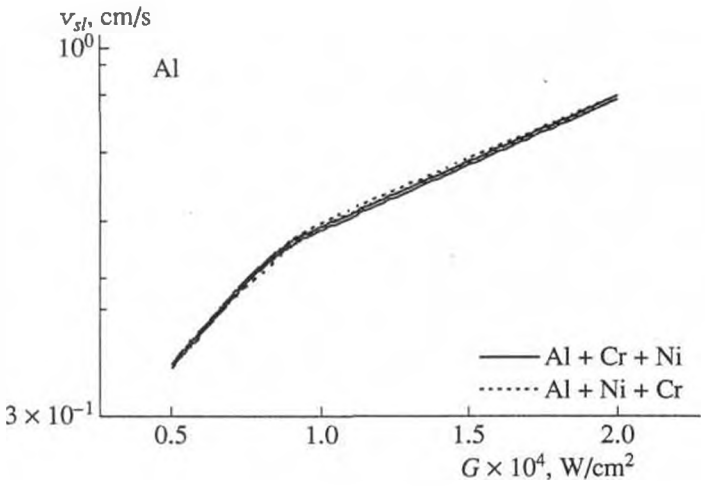

Fig. 6.

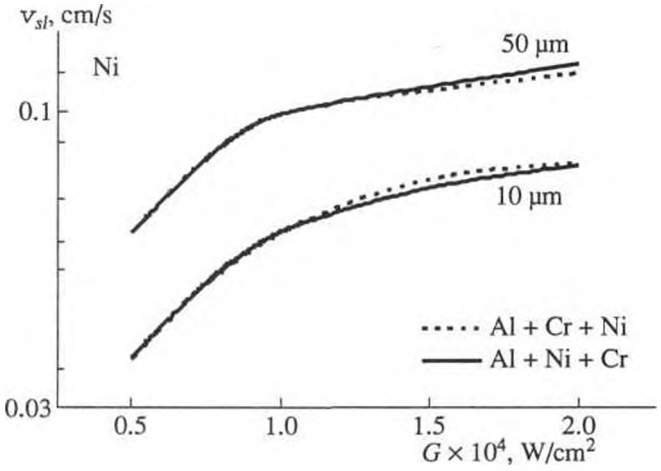

Fig. 7.

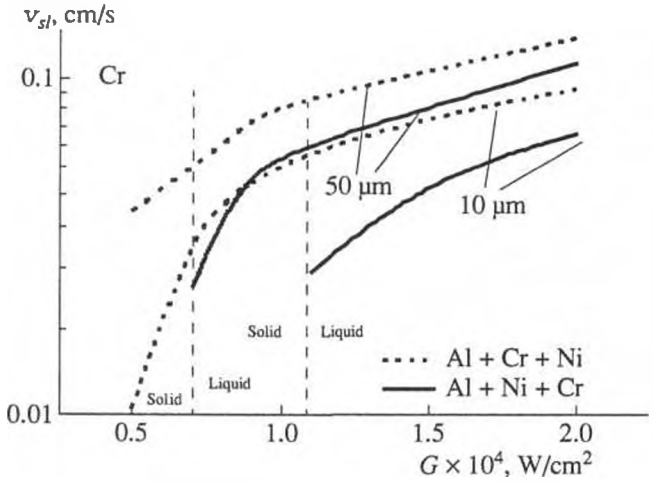

Fig. 8.

ing at $t \approx 3$ s), the surface sublimation of chromium (i.e., its evaporation from the solid phase) starts with the rate $v_{lv,\max} \approx 7.6 \times 10^{-3}$ cm/s. By $t = 3.6$ s, when approximately 92.8% of the chromium has evaporated, it starts to melt, and then completely evaporates from the liquid phase shortly before the end of the pulse at $t \approx 3.75$ s (see Fig 4a). This effect is not observed in the configuration depicted in Fig. 1b, where the exposed layer consists of nickel (see Fig. 4b). Nickel starts to evaporate later than chromium (at $t \approx 3.5$ s) and the maximum evaporation rate is half of that for chromium ($v_{sl,\max} \approx 3.6 \times 10^{-3}$ cm/s).

We also note that even though the laser pulse has a rectangular profile, the heating and phase transitions for both variants are strongly nonstationary. The maximum temperature $T_{\max} \approx 2247$ K on the surface of chromium is attained by the moment of complete evaporation; for nickel, the maximum temperature $T_{\max} = 2300$ K is attained by the end of the laser pulse (see Fig. 5). Due to the higher evaporation rate, the maximum temperature on the surface of chromium is somewhat lower than on the surface of nickel.

Consider the main traits of the phase transitions in the three-layer system. From the practical point of view, the heating and phase transitions in the upper exposed layer are of primary interest. In particular, it is important to investigate the dependence of the behavior of the upper layer (which can be chromium or nickel) on its depth. It is important to determine the range of intensities and durations of the laser pulses for which the upper layer is completely evaporated.

Melting. In the range of intensities $G = (3 \times 10^5 - 2 \times 10^4)$ Wt/cm^2, the maximal melting rate for the aluminum substrate ($l = 0.5$ cm) increases with the growth of the intensity ($v^{\mathrm{Al}}_{s,l,\max} = 0.36$–$0.86$ cm s^{-1}), and it is independent of the thickness of the coatings and of the arrangement (see Fig. 6). When the thickness of the doping layers increases, only the time of attaining the maximum melting rate of the aluminum layer is delayed.

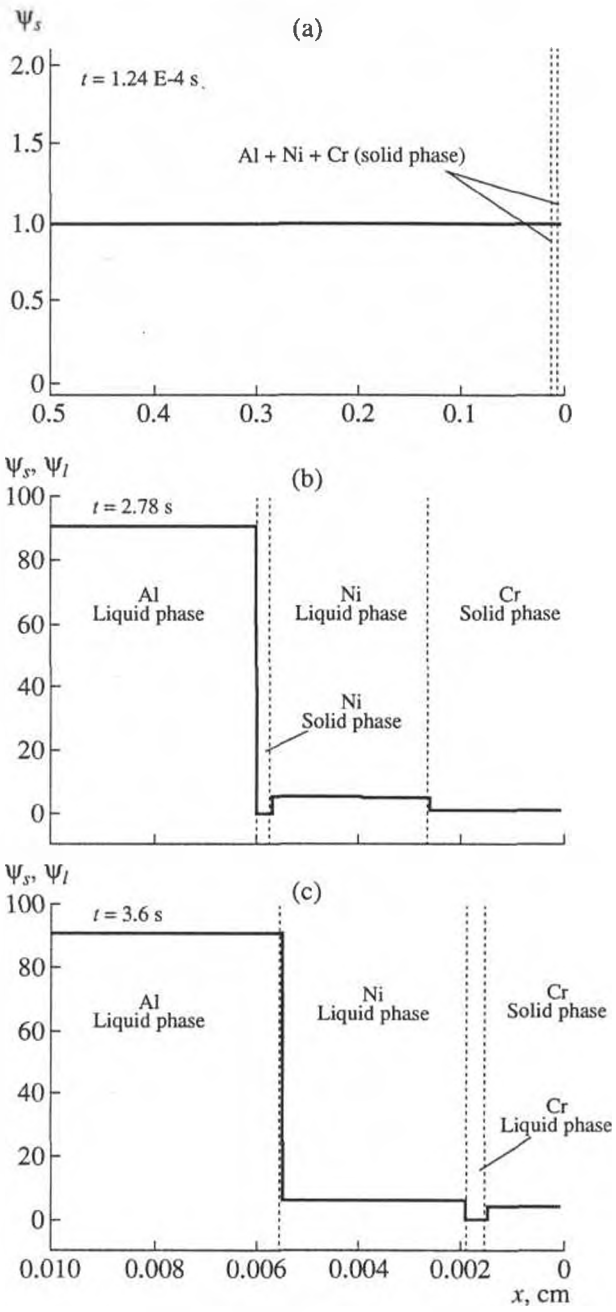

Fig. 9.

For nickel and chromium, the maximum melting rate depends not only on the intensity but also on the thickness of the layer itself (see Figs. 7, 8). If the layer is thin ($l = 10$ μm), the greater part of heat is relayed to the lower layers, which affects the melting rate. When the thickness is increased to $l = 50$ μm, the heat flows in the layer become less intensive, and the melting rate $v_{sl,\max}$ increases. For example, for nickel, $v_{sl,\max}$ increases by a factor of 2–3 (see Fig. 7), while the melting rate is almost independent of the location of the layer; i.e., it is of no importance whether nickel is the upper or the lower layer. For the chromium layer (see Fig. 8), the behavior strongly depends on the location of the layer. If the upper layer consists of chromium and is thin ($l \sim 10$ μm), it has enough time to completely evaporate before the melting starts (see Fig. 8).

The dynamics of melting for each of the layers can be described by the functions ψ_s and ψ_l. These function show how many times the size of the solid and the liquid phases change under the influence of the moving melting fronts. Figure 9 shows the space distribution of ψ_s and ψ_l for several instants of time. We assume

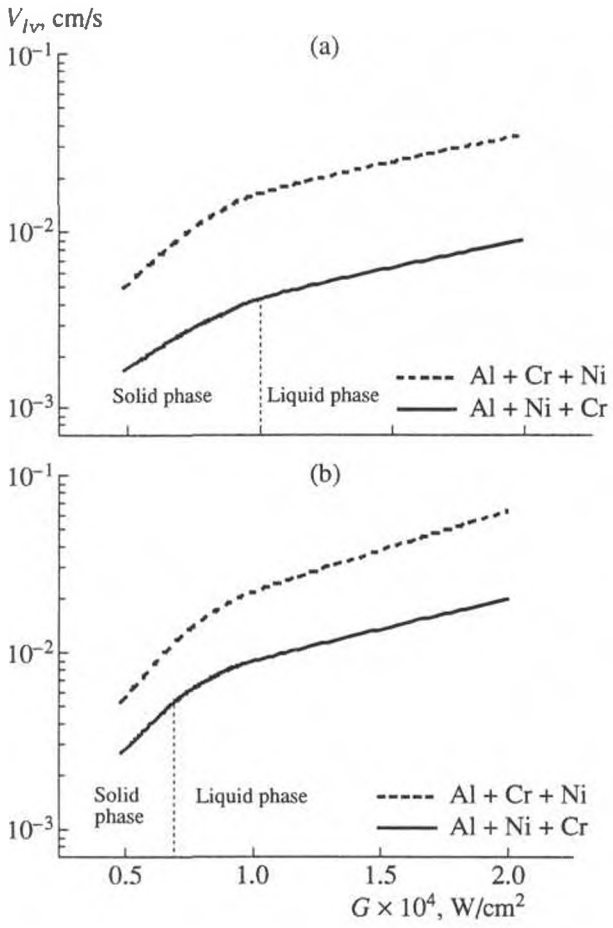

Fig. 10.

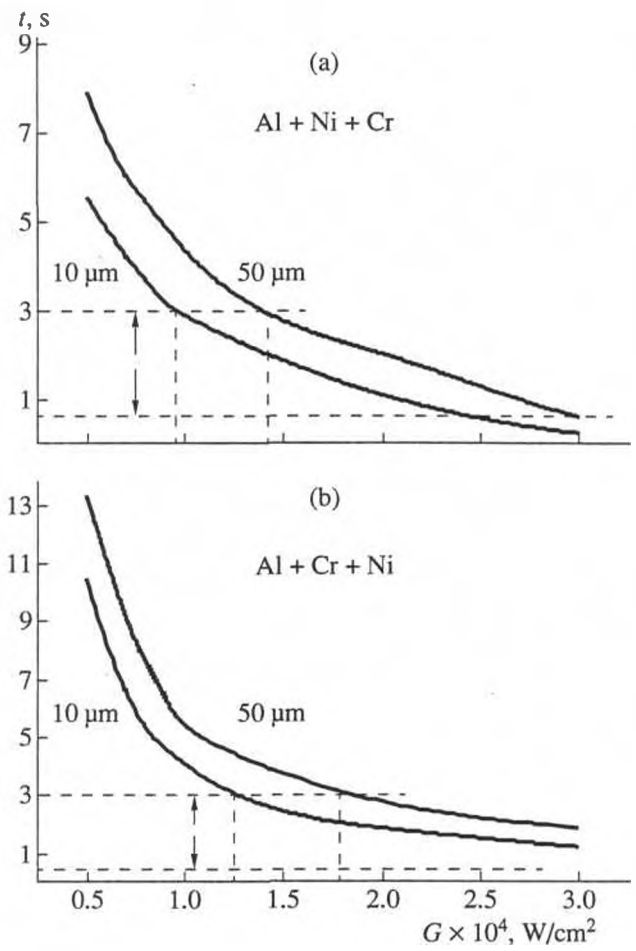

Fig. 11.

that the sizes of the physical and computation spaces are identical at the initial time $t = 0$; therefore, $\psi_s(0, x) = 1$. This relation remains valid up to the moment when the aluminum begins to melt, i.e., up to $t = 1.24 \times 10^{-4}$ s (see Fig. 9); at this time, the region occupied by the solid phase begins to shrink, i.e., $\psi_s(t, x) < 1$, until it completely vanishes ($\psi_s(t, x) = 0$). At the same time, the region occupied by the liquid phase begins to grow up to its maximal size $\psi_{l,\mathrm{Al}}(t, x) \approx 92$ (see Fig. 9b). Later, the function $\psi_{l,\mathrm{Al}}(t, x)$ remains invariable up to the beginning of crystallization because $v_{sl} = 0$. Figure 9b also illustrates the melting of nickel: $\psi_{s,\mathrm{Ni}}(t, x) \ll 1$, $\psi_{l,\mathrm{Ni}}(t, x) \gg 1$. For chromium, we have $\psi_{s,\mathrm{Cr}}(t, x) = 1$, because the melting has not yet started. The distribution of $\psi_s(t, x)$ and of $\psi_l(t, x)$ at $t = 3.6$ s (see Fig. 9c) corresponds to the stage when the aluminum and the chromium have already completely melted and the chromium is in the process of melting, which is characterized by the inequalities $\psi_{s,\mathrm{Cr}}(t, x) \ll 1$ and $\psi_{l,\mathrm{Cr}}(t, x) \gg 1$.

Evaporation. Due to its thermophysical properties, chromium evaporates much more intensively than nickel. Figure 10 shows the dependence of the maximal evaporation rate for chromium and nickel on the intensity of the laser pulse for the thickness $l = 10$ and $l = 50$ μm; these values of the thickness correspond to the minimal and maximal thickness of the coatings used in the experiments described in [4–7]. In the entire range of intensities $G = (3–30) \times 10^3$ W/cm^2, the evaporation rate for chromium is by a factor of 3–5 greater than that for nickel. The higher evaporation rate affects the time needed to completely remove the exposed layer.

Figure 11 shows the dependence of the time needed to completely remove the chromium and nickel $t_v(G)$ on the intensity of the laser pulse for two values of the thickness $l = 10$ and $l = 50$ μm.

Simulation showed that the removal of chromium by second-long and subsecond-long pulses can occur in two significantly different modes:

(a) at low intensities $G < 10^4$ W/cm^2, it occurs in the form of sublimation, i.e., in the form of evaporation from the solid phase;

(b) at higher intensities $G \geq 10^4$ W/cm^2, it occurs in the form of evaporation from the liquid phase.

For nickel, the main removal mechanism is the evaporation from the liquid phase.

In Fig. 11, the range of the duration of the laser treatment $\tau_l = 0.7$–3 s corresponding to the results described in [4–7] is marked by two horizontal dotted lines. The intersection of these lines with the curves $t_v(G)$ determines the values of $G(t)$ needed to completely remove the upper layer. For the thin chromium layer with $l = 10$ μm (Fig. 11a), this range is $9 \times 10^3 \leq G(t) \leq 2.4 \times 10^4$ W/cm^2. When the thickness is $l = 50$ μm, this range moves to the right and becomes $1.4 \times 10^4 \leq G(t) \leq 2.9 \times 10^4$ W/cm^2. If the exposure time $t \in (0.67$–$3.0)$ s and the intensity is less than the threshold values $G(t) \leq 9.0 \times 10^3$ W/cm^2 for $l = 10$ μm and $G(t) \leq 1.4 \times 10^4$ W/cm^2 for $l = 50$ μm, the chromium layers are not completely removed.

Figure 11b shows the corresponding results for nickel. Here, the situation is qualitatively different. As in the case of chromium, there are threshold values of intensity which, when exceeded, ensure that the nickel layers are completely removed: $G(t) \leq 1.3 \times 10^4$ W/cm^2 for $l = 10$ μm and $G(t) \leq 1.9 \times 10^4$ W/cm^2 for $l = 50$ μm. However, whereas the chromium layers are completely removed for any duration of the exposure, nickel is not removed for all the durations in the range $t \in (0.67$–$3.0)$ s. For $l = 10$ μm, the nickel layer is not completely removed even for the maximum intensity $G \cong 3 \times 10^4$ W/cm^2 if the exposure duration is $\tau_l \leq 1$ s; for $l = 50$ μm, this duration is $\tau_l \leq 1.5$ s. Thus, when nickel is removed by varying the exposure duration τ_l, the coating can be retained even for the maximal intensity, while this is impossible for chromium.

The results obtained can be used in designing the technology of applying multicomponent coatings and their subsequent melting. In particular, it is not advisable to make the last layer consisting of chromium.

6. CONCLUSIONS

(1) The dynamic adaptation method makes it possible to perform mathematical simulations of the phase transitions in multilayer systems. The results show that the heating of three-layer targets and the phase transitions in them are much more complicated than in homogeneous materials. Independently of the time profile and the exposure duration, three-layer systems never reach a stationary state, which is observed in homogeneous targets under the action of rectangular pulses of corresponding duration.

(2) A method for determining the diffusion coefficient is proposed that makes it possible to solve multifront Stefan problems without using fitting parameters.

(3) The simulation of the dynamics of the phase transitions in the three-layer Al + Ni + Cr targets showed that the high intensity of chromium evaporation can result in a situation when one of the doping materials is completely removed in the process of melting. Understanding the mechanism of this phenomenon may be used to theoretically justify and improve coating technology.

ACKNOWLEDGMENTS

This work was supported by the Russian Foundation for Basic Research, project no. 04-01-00701a.

REFERENCES

1. N. N. Rykalin, A. A. Uglov, I. V. Zuev, and A. N. Kokora, *Laser and Electron-Beam Treatment of Metals* (Mashinostroenie, Moscow, 1985) [in Russian].
2. V. I. Volgin, "Influence of Surface Laser Doping on the Hardness of the Aluminum Alloy AL25," Poverkhnost', Fiz., Khim., Mekh., No. 1, 125–129 (1983).
3. A. N. Safonov, A. G. Grirgo'yants, N. A. Makusheva, and A. V. Sergeev, "Investigation of the Microstructure of Aluminum and Copper Alloys Treated by the Continuous CO_2 Laser," Elektron. Obrab. Mater., No. 1, 26–29 (1984).
4. I. F. Deriglazova, I. I. Levites, and B. F. Mul'chenko, "Laser Doping of of Aluminum Piston Alloys: Investigation of the Structure," Avtomobil. Prom., Lazern. Obrab., No. 12, 8–10 (1985).
5. I. F. Deriglazova, I. V. Bogolyubova, and B. F. Mul'chenko, "Investigation of Doping Aluminum Pistons Using Laser Emission," in *Trudy of NPO NIITavtoprom* (NPO NIITavtoprom, Moscow, 1987), No. 2, pp. 33–34 [in Russian].
6. I. F. Deriglazova, B. F. Mul'chenko, S. S. Vorob'ev, et al., "Laser Hardening of Grooves in Aluminum Pistons," Avtomobil. Prom., Tekhnologiya, Materialy, No. 9, 25–26 (1987).

7. I. V. Bogolyubov, I. F. Deriglazova, and B. F. Mul'chenko, "Laser Surface Doping of the Alloy AL25," Metallovedenie Term. Obrab. Metal., No. 5, 24–25 (1988).
8. V. I. Mazhukin and A. A. Samarskii, "Mathematical Modeling in the Technology of Laser Treatments of Materials," Surv. Math. Ind. **4**, 85–149 (1994).
9. N. A. Dar'in and V. I. Mazhukin, "Mathematical Modeling of the Stefan Problem on an Adaptive Grid," Differ. Uravn. **23**, 1154–1160 (1987).
10. P. V. Breslavskii and V. I. Mazhukin, "Mathematical Modeling of Pulse Melting and Evaporation of Metals with the Explicit Tracking of the Interphase Boundaries," Inzh. Fiz. Zh. **57** (1), 107–114 (1989).
11. V. I. Mazhukin, I. Smurov, C. Dupuy, and D. Jeandel, "Simulation of Laser Induced Melting and Evaporation Processes in Superconducting Ceramics," J. Numer. Heat Transfer, Part A **26** 587–600 (1994).
12. B. Cheynet, J.-D. Dubois, and M. Milesi, "Données thermodynamiques des éléments chimiques," in "Technique de l'ingenier, traité materiaux metalliques" (Imprimerie Strasbourgeoise, Strasbourg, 1993), pp. M 64-1–M 64-22.
13. M. Laurent and P. L. Vuillermoz, "Conductivité Thermique des Solides," in "Technique de l'ingenier, traité constantes physico-chimiques" (Imprimerie Strasbourgeoise, Strasbourg, 1995), pp. K 420-1–K 420-30.
14. *Numerical Data and Functional Relationships in Science and Technology*, Ed. by H. von Borchers and E. Schmidt (Springer, Berlin, 1964), Vol. 6.
15. *Metals Reference Book*, Ed. by C. J. Smithells (Butterworth, London, 1976; Metallurgiya, Moscow, 1980).
16. *Physical Quantities: Handbook*, Ed. by I. S. Grigor'ev and E. P. Melikhov (Energoatomizdat, Moscow, 1991).
17. *Zahlenwerte und Funktionen aus Physik, Chemie, Astronomie, Geophysic und Technik*, Vol 2: *Eigenschaften der Materie in ihren Aggregatzuständen*, Ed. by J. von Bartels, H. von Borchers, and P. Tens (Springer, Berlin, 1961).
18. A. N. Tikhonov and A. A. Samarskii, *Equations of Mathematical Physics* (Mosk. Gos. Univ., Moscow, 1999) [in Russian].
19. A. A. Samarskii, *Theory of Finite Difference Schemes* (Nauka, Moscow, 1977; Marcel Dekker, New York, 2001).
20. A. A. Samarskii and E. S. Nikolaev, *Methods for Solving Difference Equations* (Nauka, Moscow, 1978) [in Russian].